ABSTRACT

Title of Thesis:	DEVELOPMENT OF A PYROLYSIS MODEL FOR ORIENTED STRAND BOARD
	Hongen Zhou, Master of Science, 2021
Thesis Directed By:	Dr. Stanislav Stoliarov, Professor, Department of Fire Protection Engineering

Oriented Strand Board (OSB) is a widely used construction material responsible for a substantial portion of the fire load of many buildings. To accurately model the response of OSB to fire, Thermogravimetric Analysis (TGA), Differential Scanning Calorimetry (DSC) and Microscale Combustion Calorimetry (MCC) tests were carried out to construct a thermal decomposition model using a numerical solver, ThermaKin2Ds, and a hill climbing (*HC*) optimization algorithm. The model was determined to consist of two distinct processes. The first process is a single step water vaporization. The second process is a chain of four consecutive reactions representing thermal decomposition of the organic constituents of OSB. The experiments and modeling revealed that the first two of the four reactions are endothermic, while the last two are exothermic, and that the net heat of decomposition is near zero. The heat capacities of condensed-phase species and heats of combustion of evolved gases were also determined from inverse modeling of the DSC and MCC tests, respectively. Controlled

Atmosphere Pyrolysis Apparatus II (CAPA II) experiments were performed at 35 kW m^{-2} and 65 kW m^{-2} of the radiant heat flux. The sample bottom temperature data obtained at 65 kW m^{-2} were used to determine the thermal conductivities of condensed-phase species. The complete pyrolysis model of OSB was subsequently validated by comparing the experimental CAPA II mass loss rate profiles with the model predictions. The undecomposed OSB density was found to vary both along the sheet surface and through thickness. However, these density variations had only a minor impact on the key features of the mass loss rate profiles.

DEVELOPMENT OF A PYROLYSIS MODEL FOR ORIENTED STRAND BOARD

by

Hongen Zhou

Thesis submitted to the Faculty of the Graduate School of the
University of Maryland, College Park, in partial fulfillment
of the requirements for the degree of
Master of Science
2021

Advisory Committee:
Professor Stanislav I. Stoliarov, Ph.D., Chair
Professor Arnaud Trouvé
Professor Peter B. Sunderland
Professor James A. Milke

Acknowledgements

First, I would like to express my sincere appreciation to Dr. Stanislav Stoliarov for his patience, advice, encouragement through the past two and half years. Thank you for your guidance throughout this project, in matters both related and unrelated to research. I could not hope for a better advisor, and you are definitely a great model for my future work.

I would like to also thank my research group for creating such a great environment to study and work. I was always motivated by your determination when I was struggling. Dushyant, Greg, and Josh, thank you for your instructions on conducting experiments. Jacques, thank you for being the one that I can always reach out to whenever I have question on both studies and researches. Conor, Lucas, and Will, thank you for your willingness to offer help. I would like also to thank Fernando and Ryan for all their technical support on preparing materials and fixing equipment malfunctions.

Next, I would like to thank Dr. Junhui Gong and Hong (Amy) Zhu for their help in performing TGA/DSC experiments and analysis. I am grateful to have had opportunity to work with them.

I would like to thank and acknowledge the committee members: Dr. Arnaud Trouvé, Dr. Peter Sunderland, and Dr. James Milke. Thank you for being flexible on your schedule and willing to give your time to review this work. I would like to acknowledge the National Institute of Standards and Technology (grant

#70NANB19H053) for the generous financial supported which made this work possible.

Finally, I would like to thank my family for their unwavering support and love. They have ingrained in me the discipline and drive to succeed and always trusted me, understanding and supporting any decision I make.

Table of Contents

List of Tables

List of Figures

Chapter 1: Introduction

1.1 Background

Oriented Strand Board (OSB) is a composite wood panel that is made of layers of compressed wood strands and adhesives. The general manufacturing process of OSB includes stranding, blending with resin and small amount of wax, orienting and formation of multi-layers structure, and pressing at a high temperature and pressure. The manufacturing of OSB does not require large-diameter logs. Therefore, fast-growing species, such as aspen, pine are commonly used as the raw materials of OSB. In addition to that, the manufacturing process of OSB can use almost every part of the wood logs. These factors bring an obvious advantage of OSB, which is its lower cost. As an economic-efficient construction material, OSB has drawn the interest of the market since it was introduced to North America in the 1960s. The mechanical performance of OSB has grown with the development of its manufacture techniques. In 1992, OSB was certified to perform as well as softwood plywood, since then, the consumption of OSB has rapidly increased from rapidly from around 5 billion square feet in 1990 to around 15.0 billion square feet by 2005 [1]. OSB has dominated the construction market as it gradually taking over the market share of plywood, and the market share of OSB grew from 43% to 66% within the last two decades [2].

OSB can be used in various ways, such as subfloors, underlayment, walls, floors, and roof sheathings, and could be found in most buildings in North America.

The widespread popularity of OSB has drawn increased safety concerns regarding its nature as a potential fire hazard related to the carbon-based nature of the material. In some buildings, especially low-rise residential buildings, OSB has become one of their major fire loads. In Wildland–Urban Interface (WUI) fires and urban fires, it was found that the building structure themselves could be a large source of firebrands [3], which is a significant cause of structure ignition and fire spread. Despite the developments of multiple mechanical performance standards for OSB, the material's pyrolysis is still relatively unexplored, and thus being able to determine how OSB contributes to fire growth in given scenarios is of utmost importance.

1.2: Literature review

The study of pyrolysis of composite materials, such as engineered wood products (EWPs), has attracted lots of attention in past a few decades. An inverse analysis of thermogravimetric analysis (TGA) test results has become a common procedure to determine the kinetic parameters of decomposition for pyrolyzable solids. Purnomo et al. [4] reviewed several studies in kinetic inverse modeling and summarized this process into five steps, including acquire TGA experimental data, choose chemical kinetic model for prediction, calculate the error between experimental data and prediction, formulate the error using different object functions, and minimize the error using optimization algorithms.

As composite materials, the decomposition of wood or EWP were defined in different ways in different studies. Shafizadeh and Chin [5] described the wood pyrolysis as one-component reaction, that the wood would be pyrolyzed into three components, char, tar, and combustible volatiles. Another common mechanism of

decomposition of wood is multiple-component scheme, which is usually a three-components scheme for wood, where the wood is assumed consisted of three components, hemicellulose, cellulose and lignin. This scheme assumes that there is no interaction between these components, and three reactions occur in parallel.

Using this scheme and composition of wood, Grønli et al. [6] collected the TGA data of four different hardwoods and five different softwoods and proposed a common decomposition mechanism of them. Besides these common components, Li et al. [7] examined the medium density fiberboard (MDF) with an additional component, resin, and came up with a four-step parallel reaction scheme. Using genetic algorithm (GA), the kinetic parameters and the initial fraction of each component were determined. Instead of specifying the exact components, Ira et al. [8] used sets of three or four parallel reactions to simulate the decomposition of several EWPs including plywood, OSB, particle board (PB), and MDF, and used shuffled complex evolution (SCE) optimization algorithm to obtain the kinetic parameters and the initial fraction of each component. The parallel reactions were expressed below:

$$v_{X,j}X \rightarrow v_{R,j}R + volatiles \tag{1}$$

$$r_j = A_j e^{(\frac{-E_j}{RT})} y_X^{n_j} \tag{2}$$

Equation (1) represents the parallel reactions adopted in Ira's study, where X is reactant, R in equation (1) denotes a solid residue, and v is stoichiometric coefficient of reactant or solid residue in reaction j. Equation (2) represents the reaction rate involves the kinetic parameters, where j and X denote the reaction j, and reactants X. r is the rate of reaction, A is Arrhenius pre-exponential factor, E is activation energy, R is the Boltzmann constant, T is temperature, y is the mass

fraction of reactant over its initial mass, and *n* is the reaction order. All the results from Li et al. [7] and Ira et al. [8] were summarized in Table 1.

Table 1. Kinetic parameters of several EWPs

Material		Reaction 1	Reaction 2	Reaction 3	Reaction 4
Plywood[8]	$\log A_j$ [log 1/s]	21.0	7.4	19.4	6.1
4 equations	E_j [kJ /mol]	236	107	254	91
	n [-]	1.5	1.2	1.5	4.0
	$y_{j,0}$ (%)	2.0	38.0	45.6	14.4
	v_j [-]	0.216	0.216	0.216	0.216
Plywood[8]	$\log A_j$ [log 1/s]	8.6	23.3	6.7	-
3 equations	E_j [kJ /mol]	119	299	85	-
	n [-]	1.3	1.5	5.0	-
	$y_{j,0}$ (%)	39.2	41.6	19.2	-
	v_j [-]	0.216	0.216	0.216	-
OSB[8]	$\log A_j$ [log 1/s]	7.6	25.4	2.7	-
	E_j [kJ /mol]	112	326	56	-
	n [-]	1.2	1.5	3.1	-
	$y_{j,0}$ (%)	39.8	34.8	25.4	-
	v_j [-]	0.236	0.236	0.236	-
PB[8]	$\log A_j$ [log 1/s]	7.2	23.7	1.8	-
	E_j [kJ /mol]	107	304	45	-
	n [-]	1.2	1.5	2.8	-
	$y_{j,0}$ (%)	36.8	34.1	29.1	-
	v_j [-]	0.274	0.274	0.274	-
MDF[8]	$\log A_j$ [log 1/s]	7.4	10.2	22.5	1.5
	E_j [kJ /mol]	74	134	287	45
	n [-]	3.1	1.6	1.5	2.4
	$y_{j,0}$ (%)	8.1	31.3	37.4	23.2

	v_j [-]	0.245	0.245	0.245	0.245
MDF[7]		Reaction of resin	Reaction of hemicellulose	Reaction of cellulose	Reaction of lignin
	$logA_j$ [log 1/s]	13.6	12.9	13.6	16.3
	E_j [kJ /mol]	149	165	189	238
	n [-]	4.7	2.4	0.84	10.4
	$y_{j,0}$ (%)	9.9	31.7	40.8	17.6
	v_j [-]	0.116	0.115	0.248	0.272

Their modeled results provided a good fit for experimental mass loss rate (MLR) on all EWPs, however, failed to capture some small MLR peaks. Most obvious visual discrepancies were observed for plywood, where both three steps and four step models failed to accurately capture MLR maxima and minima. A better fit was obtained by Fateh et al. [9] who used three consecutive reactions to describe the decomposition of plywood, which suggests that consecutive reaction scheme may provide a more accurate description of the thermal decomposition of wood products than parallel reaction scheme.

Thermodynamic parameters, including heats of individual decomposition steps and heat capacities of the condensed-phase reactants and products, have also been shown to be important for accurate pyrolysis modeling [10]. Li and Stoliarov [11 - 12] first demonstrated how these properties can be derived from DSC experiments that were conducted simultaneously with TGA tests. McKinnon et al. [13 - 14] and Ding et al. [15] extended this analysis by fully accounting for variation in instantaneous heating rate observed in TGA/DSC experiments and including the

MCC testing and inverse modeling to obtain heats of combustion of individual gaseous products defined in multi-step reaction mechanisms.

Thermal conductivity is another important parameter for material analysis and pyrolysis modeling. Multiple studies have been done to determine the thermal conductivity of EWPs using various apparatuses, such as HC-072 thermal conductivity tester [16] and TCi thermal conductivity analyzer [17] amongst others. The majority of apparatuses employ the same methodology, where the thermal conductivity of the material is derived from the measured temperature difference at different spots of the test sample. Studies have also found that the thermal conductivity of EWPs is greatly affected by external factors such as moisture content and temperature. Kawasaki and Kawai [16] measured the thermal insulation properties of plywood, MDF, particle board (PB), OSB and solid wood using HC-072 thermal conductivity tester, which was designed according to the Japanese Industrial Standard (JIS A1412) and the American Society of Testing Materials (ASTM C518). Kamke [18] studied the thermal conductivities of several EWPs, including PB, MDF, and two types of OSB with different thicknesses, and concluded that there is little or no effect of the thickness on the thermal conductivity of OSB, and the moisture content and material density will affect the thermal conductivity of these commercial wood panels, with both factors mostly having a positive correlation with thermal conductivity. Sonderegger and Niemz [19] had concurring results, concluding that the thermal conductivity increased by 1-2% per percent increase of moisture content and there is no clear correlation between the thickness and the thermal conductivity of OSB. However, their results did not show a clearly higher thermal conductivity of

OSB sample who has a greater density. Czajkowski and co-authors [20] utilized inverse analysis to extract the thermal conductivity of OSB, low density fiberboard (LDF), and PB, and derived two expressions for both transverse thermal conductivity and in-plane thermal conductivity of each material with the first being a constant value independent of temperature, and the second being a linear temperature dependence correlation. The thermal conductivities of these studied EWPs were summarized in Figure 1.

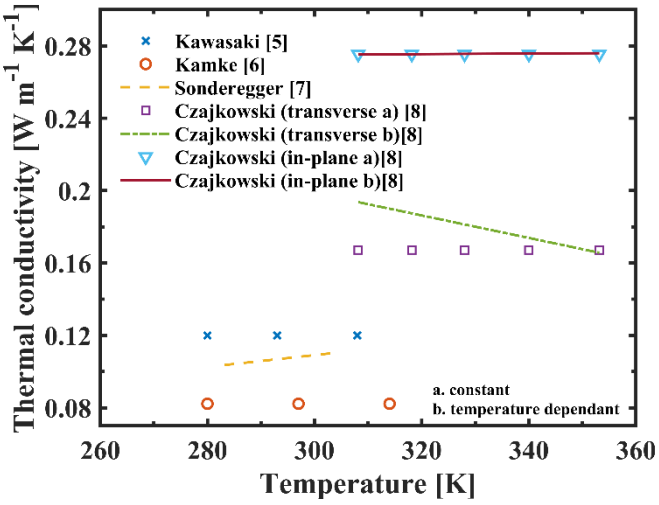

Figure 1. Comparison of thermal conductivities of OSB from different studies.

Most of these studies focused on the how moisture content and material density would affect the thermal conductivity [18, 20], and Sonderegger and Niemz [19] and Czajkowski et al. [20] also considered the impact of temperature on the thermal conductivity. However, as shown in figure 1, there is a large variation between these results. This large variation might be explained by different materials or measuring techniques. However, directly adopting any of these results in the pyrolysis model might be unreliable.

Except for directly measuring the thermal conductivity, McKinnon [21] determined the thermal conductivity of multiple composites by conducting bench-scale tests using CAPA, and inverse analyzing the experimental temperature results using ThermaKin.

The absorptivity/emissivity of several EWPs were also studied, with Agarwal et al. [22] 's research finding that the emissivity functions of plywood and MDF closely resembled each other, as well as both being temperature dependent. Försth and Roos [23] also studied the absorptivity of plywood and other wood products under different temperatures of the radiation source. A general pattern was found that the absorptivity of the materials they studied would decrease as the temperature of the radiation source increases. They also measured the absorptivity of these materials after different exposure time under cone calorimeter, and their results showed that the dependance of absorptivity on the exposure time differs from materials, and for most wood products, a slightly decreasing trend was found as the exposure time increases.

1.3 Motivation

Li et al. [7] and Ira et al. [8] have determined the kinetic parameters of several EWPs, including OSB. However, the decomposition thermodynamics and the thermal conductivity of solid components were not studied, and the heats of combustion for individual gaseous products were not resolved in their studies. Their results also showed a large difference between the kinetic parameters of different EWPs.

Large variation was also observed in the thermal conductivities between different EWPs and even within different studies' results on the same material, OSB. Most of these measurements failed to take the decomposition of OSB into

consideration and were conducted at a relatively low temperature. These preset parameters render the results unable to accurately express the thermal conductivity of OSB in situations involving high temperatures, such as during a fire.

This study aims to develop a more complete understanding of OSB pyrolysis by determining its kinetic parameters, decomposition thermodynamics, heats of combustion for individual gaseous products, as well as finding a representative model describing the thermal conductivity of the OSB and its solid pyrolysis products. Such improved understanding is expected to enable a more accurate modeling of fire growth in residential structures, where OSB is used in significant quantities.

1.4 Approach

McKinnon [13 – 14, 21, 24] developed a generalized methodology to develop a pyrolysis model for composite materials which was adopted in many later studies. A complete pyrolysis model usually includes the reaction mechanism, the kinetic parameters, thermodynamic parameters including the heats of decomposition, and physical parameters including thermal conductivity and density of a material. This methodology employs milligram-scale tests and bench-scale tests and inverse analyzing of the experimental data to generate the needed parameters for a pyrolysis model. The overall methodology was later adopted and developed by Swann [25-28] to characterize pyrolysis of synthetic polymers. The developed methodology was recently automated by Fiola e al. [29], and a similar methodology will be used in this study.

In the current study, a thorough characterization of the thermal decomposition and thermal transport inside the OSB was performed using experimental and

numerical modeling techniques. The experimental techniques included TGA/Differential Scanning Calorimetry (DSC) and Microscale Combustion Calorimetry (MCC) milligram-scale tests and Controlled Atmosphere Pyrolysis Apparatus II (CAPA II) gram-scale tests. The milligram-scale tests provided a quantitative measurement of the sample mass loss, heat flow, and heat release rate associated with the combustion of pyrolyzate gases released during anaerobic thermal decomposition of a solid sample under controlled temperature conditions. The gram-scale (CAPA II) tests provided well-defined boundary conditions and highly resolved measurements of mass, shape and surface temperature of a coupon-sized solid sample exposed to a set radiant heat flux.

A hill climbing (*HC*) optimization algorithm implemented as a MATLAB script [29] was used in conjunction with ThermaKin2Ds, a previously developed numerical comprehensive pyrolysis solver [25, 30], to perform inverse analysis of the experimental datasets and determine the kinetic parameters and thermodynamics of the OSB decomposition as well as its thermal transport properties. The fully parameterized comprehensive pyrolysis model was validated by comparing the CAPA II MLR profiles obtained at two radiant heat flux settings and surface temperature profile obtained at one heat flux setting with the model predictions.

Chapter 2: Experimental Methods

2.1 Sample preparation and density measurements

Tested samples were taken from 7/16 CAT Georgia-Pacific Blue Ribbon PS2-10-compliant OSB panels purchased from Lowe's. Parts of the OSB were grounded into fine powder for milligram-scale tests. 7 cm diameter disks were cut from the panels for CAPA II tests. All samples were conditioned in a desiccator in the presence of Drierite for 24 hours to achieve a consistent and a low moisture content.

The density of the dried OSB was calculated at room temperature by measuring dimensions and mass of a set 0.2×0.2 m^2 samples cut from various panel locations. The density variation through thickness was also examined by sanding about 1/4 of the sample thickness and measuring the resulting changes in mass and volume. The sending was performed on both sides of each sample so that three density measurements were obtained across thickness.

2.2 Milligram-scale tests

2.2.1 Simultaneous thermal analysis (STA)

The TGA (thermogravimetric analysis) and DSC (differential scanning calorimetry) tests were conducted using a Netzsch 449 F3 Jupiter STA, which can record sample mass and heat flow as a function of temperature and time as the sample is heated up at a prescribed heating rate. The mass of OSB powder used in each test was around 6 mg. Ten repeated tests was performed using platinum-rhodium

crucibles with lids at a heating rate of 10 K min^{-1} in nitrogen atmosphere to determine the decomposition mechanism and relevant kinetic and energetic parameters. Six additional TGA-only tests were performed at a heating rate of 5 K min^{-1} and 20 K min^{-1} in triplicate using open ceramic crucibles. These test results were used to ensure that the thermal decomposition model parameterized based on 10 K min^{-1} tests performed well at alternate heating rates. Five additional TGA/DSC tests were performed at 10 K min^{-1} on the char residue collected from the TGA/DSC experiments on undecomposed OSB to determine heat capacity of this residue.

2.2.2 Microscale Combustion Calorimetry (MCC)

MCC testing of OSB samples was performed in accordance with the corresponding ASTM standard [31] in an apparatus calibrated weekly following the recommended protocols [32]. The initial mass of the sample was about 5 mg. The sample was conditioned for 2 min at 348 K and heated with a nominal heating rate of 10 K min^{-1} to 1000 K. Similarly to the TGA/DSC tests, the sample was pyrolyzed in nitrogen atmosphere. The gaseous pyrolyzate was mixed with excess oxygen in a high temperature combustor maintained at 1173 K to achieve complete or nearly complete combustion. The oxygen concentration decline in the exhaust gas flow was measured by a calibrated oxygen sensor. The heat release rate (*HRR*) was subsequently calculated using the oxygen consumption principle [32] and recorded as a function of time and pyrolyzing sample temperature. This test was repeated only 3 times because its results were found to be highly repeatable.

2.3 Gram-scale tests - Controlled Atmosphere Pyrolysis Apparatus II (CAPA II) tests

The Controlled Atmosphere Pyrolysis Apparatus II (CAPA II) is an apparatus that can be used to analyze material pyrolysis. Figure 2 shows a schematic of the CAPA II. The apparatus consists of a temperature controlled conical radiant heater that is placed above a disk-like solid sample at the start of a test. The sample is located inside a water-cooled gasification chamber, which was continuously purged with 185 SLPM of nitrogen in the current tests to create an anaerobic environment within the chamber [33].

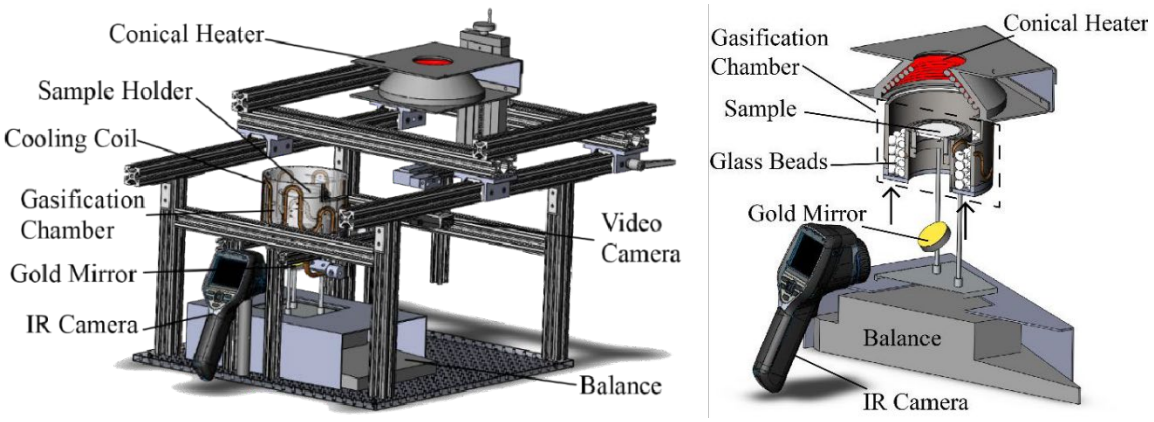

Figure 2. Drawing of the controlled atmosphere pyrolysis apparatus II (CAPA II) [33].

The CAPA II diagnostics include three main components: mass, back surface temperature (T_{back}) and sample shape. The instantaneous mass of the sample is recorded using a high precision (1 mg resolution) Sartorius Cubis balance at a frequency of 2 Hz. A FLIR E40 infrared (IR) camera is focused on the thin copper foil holding the sample to measure the T_{back} at a frequency of 7.5 Hz. The foil is coated with a high (0.92) emissivity paint to ensure accuracy of this measurement.

Due to geometrical constraints, a gold mirror (with average reflectance of 0.96) is used to provide the view to the back of the sample. The emissivity in the IR camera was adjusted to account for the transmission loss in the gold mirror, and was validated against thermocouple based temperature measurements. A Logitech C930e high definition camera is focused on the sample through a quartz observation window to monitor evolution of the sample surface position. In addition, a fine thermocouple is positioned within the channel between the aluminum tubes, above the glass beads, to provide continuous reading of the flowing gas temperature. One more thermocouple is used to monitor the temperature of the inner wall of the aluminum tube facing the back of the sample.

In the current CAPA II tests, the side surfaces of 7-cm-diameter OSB samples were insulated with rings made out of Kaowool PM ceramic fiber board. The samples were attached to the copper foil using a small amount of high temperature epoxy to improve thermal contact between the sample the foil. The CAPA II tests were performed at two heater settings of 35 kW m^{-2} and 65 kW m^{-2}.

Chapter 3: Modeling methods

3.1 Modeling of milligram-scale tests

The STA and MCC samples were represented in the model as thermally thin and simulated with ThermaKin2Ds using a single spatial element. The element temperature was forced to follow the experimental temperature profile by defining a sufficiently high convection coefficient, 1×10^5 W m^{-2} K^{-1}, at the boundary. As shown in Figure 1, the sample heating rates observed in the experiments varied considerably before reaching the nominal (or set) values. To take these variations into account, the modelled heating rate was expressed via an exponentially decaying sinusoidal function of the form:

$$\frac{dT}{dt}(t) = a_1\{1 - exp(-a_2 t)[cos(a_3 t) + a_4 sin(a_3 t)]\} \quad (3)$$

where a_1 (K s^{-1}), a_2 (s^{-1}), a_3 (s^{-1}) and a_4 are constants fitted to capture experimental data, T is temperature, and t is time from the start of the test. The values of the constants are summarized in Table 2. The resulting fits are shown in Figure 3. All fitted curves have the coefficient of determination larger than 0.95. The mass flow boundary conditions were defined in the model such that the gaseous pyrolyzate instantaneously escaped the element.

Table 2. Parameters describing evolution of instantaneous heating rate in the TGA/DSC and MCC tests.

Nominal heating rate	a_1 (K s^{-1})	a_2 (s^{-1})	a_3 (s^{-1})	a_4 (-)
5 K min^{-1} (TGA/DSC)	0.0834	0.00384	0.00484	-1.2338
10 K min^{-1} (TGA/DSC)	0.1670	0.00306	0.00510	-0.7544
20 K min^{-1} (TGA/DSC)	0.3245	0.00313	0.00354	-1.5110
10 K min^{-1} (MCC)	0.1686	0.00345	0.00405	-0.2617

A single goodness of fit criterion, GoF_M, was used in the *HC* algorithm as a target for optimization of the kinetic parameters of the OSB decomposition:

$$GoF_M = 1 - \left(\frac{0.6}{\mathrm{MLR}_{max,exp}} \sqrt{\frac{\sum_i^N \left(\mathrm{MLR}_{i,exp} - \mathrm{MLR}_{i,model}\right)^2}{N}} + \frac{0.4}{m_{max,exp}} \sqrt{\frac{\sum_i^N \left(m_{i,exp} - m_{i,model}\right)^2}{N}} \right) \quad (4)$$

In Eq. (4), *m* is the sample mass. The subscripts *max*, *exp* and *model* denote the maximum, experimental and modeled values, respectively. *N* is the total number of experimental data points. This criterion was formulated to obtain the best compromise between capturing both the MLR and mass profiles of a wide range of pyrolyzable solids. A GoF_M of 1 implies a perfect fit. More details on the algorithm implementation can be found in an earlier publication [29]. The corresponding DSC data and MCC data were fitted manually by adjusting condensed-phase component heat capacities and heats of reactions (in the case of DSC) and gaseous product heats of combustion (in the case of MCC) until a good agreement between the experimental and modeled data was achieved.

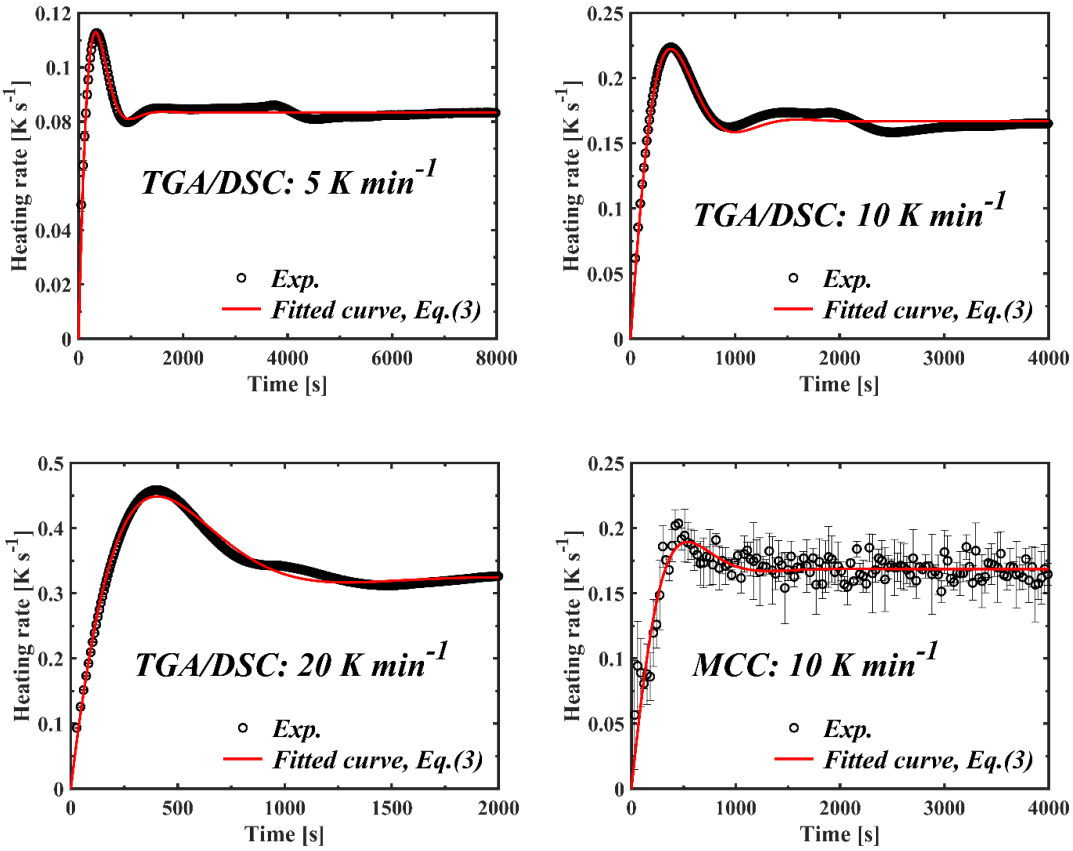

Figure 3. Averaged experimental and fitted heating rate profiles obtained for the TGA/DSC and MCC tests.

3.2 Modeling of CAPA II tests

Using the reaction mechanism and parameters derived from milligram-scale tests, CAPA II tests were simulated with ThermaKin2Ds. These simulations were set up as one-dimensional. The sample was divided into 0.05 mm thick elements. The mass and energy conservation equations, provided elsewhere [30], were integrated using 0.002 s time step to achieve convergence.

The radiation from the heater to the front sample surface was modeled using a previously defined expression [33], which took into account changes in the position

of this surface with respect to the heater. The heat exchange between the front sample surface and the gaseous environment was represented by a spatially averaged convection coefficient of 7.2 W m^{-2} K^{-1} [33] and the experimentally measured gas temperature, T^e, evolution captured with:

$$T^e = T_1^e \exp(T_2^e\, t) + T_3^e \exp(T_4^e\, t) + T_{HFG} \quad (5)$$

The parameters of this equation are summarized in Table 3. They were obtained by fitting the experimental data obtained in two representative tests at each heat flux, as shown in Figure 4. The environmental temperature at the back sample boundary, T_{bottom}, was represented by a piecewise linear expression of the form:

$$T_{bottom} = b_1 t + b_2, \quad when\ t < t_c;$$
$$= b_3, \quad when\ t \geq t_c; \quad (6)$$

The parameters used in this expression were obtained by fitting the measurements of the temperature of the inner wall of the aluminum tube facing the back of the sample, as shown in Figure 4. These parameters are summarized in Table 4. T_{bottom} was used to compute the convective heat exchange between the back sample surface and the environment using a convection coefficient of 4.0 W m^{-2} K^{-1} [33] and was also used to compute radiative heat flux from the environment to the back sample surface. Transient radiative losses from the sample to the environment through the front and back sample surfaces were also accounted in the ThermaKin2Ds [25, 30].

Table 3. Heat flux-dependent fitting parameters for Equation 5 describing the time-dependent change in the environmental temperature above the front sample surface.

Heat flux	35 kW m^{-2}	65 kW m^{-2}
T_1^e [K]	53.3	92.0
T_2^e [s^{-1}]	0.554×10^{-6}	1.9275×10^{-5}
T_3^e [K]	-33.965	-59.425
T_4^e [s^{-1}]	-10.63×10^{-3}	-9.51×10^{-3}
T_{HFG} [K]	290	290

Table 4. Heat flux-dependent fitting parameters for Equation 6 describing the time-dependent change the temperature of the inner wall of the aluminum tube facing the back of the sample.

Heat flux	35 kW m^{-2}	65 kW m^{-2}
b_1 [K s^{-1}]	0.05	0.0825
b_2 [K]	288	292
b_3 [K]	306	325
t_c [s]	360	400

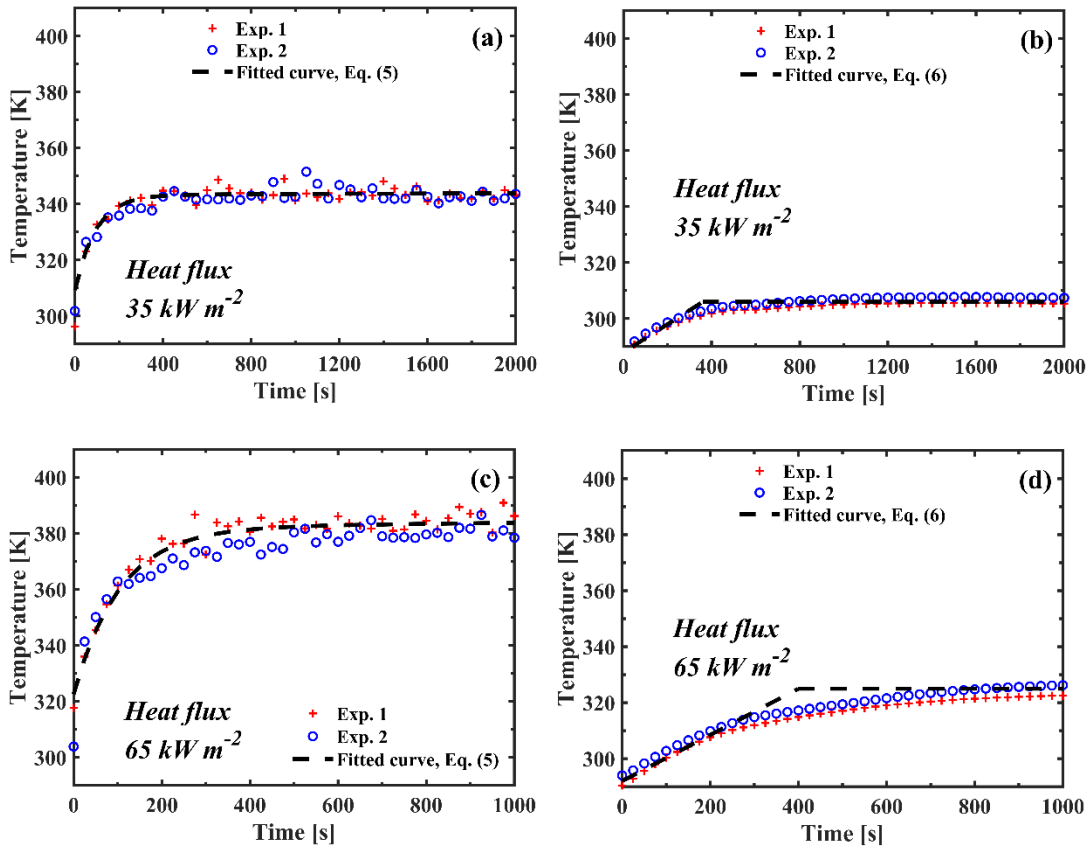

Figure 4. Mean environmental temperature histories for (a, c) the front CAPA II sample surface and (b, d) the back CAPA II sample surface obtained at 35 kW m^{-2} and 65 kW m^{-2} of incident radiant heat flux.

The optical properties of OSB and its decomposition products were defined based on the literature data, as further discussed in Chapter 4. The thermal conductivities of OSB and its decomposition products were determined through optimization using a single goodness of fit criterion, GoF_T:

$$GoF_T = 1 - \left(\sqrt{\frac{\sum_i^N \left(\frac{T_{i,model} - T_{i,exp}}{T_{i,exp}} \right)^2}{N}} \right) \quad (7)$$

In Eq. (7), $T_{i,exp}$ is the experimental back surface temperature of the sample and $T_{i,model}$ is the modeled temperature at the same time. *N* is the total number of experimental data points. A perfect fit is determined by GoF_T of 1.

Chapter 4: Results and analysis

4.1 Density measurement results

4.1.1 Density variation across OSB panel surface

The thicknesses of the OSB panels ranged between 10.6 to 11.0 mm. The mean thickness was 10.8 mm with a standard deviation of 0. 1 mm. The density was found to vary between 550 and 752 kg m^{-3} for samples cut from different areas of a panel. The mean density was determined to be 664 kg m^{-3} with a standard deviation of 56 kg m^{-3}. The density variation across a panel surface is further illustrated in Figure 5.

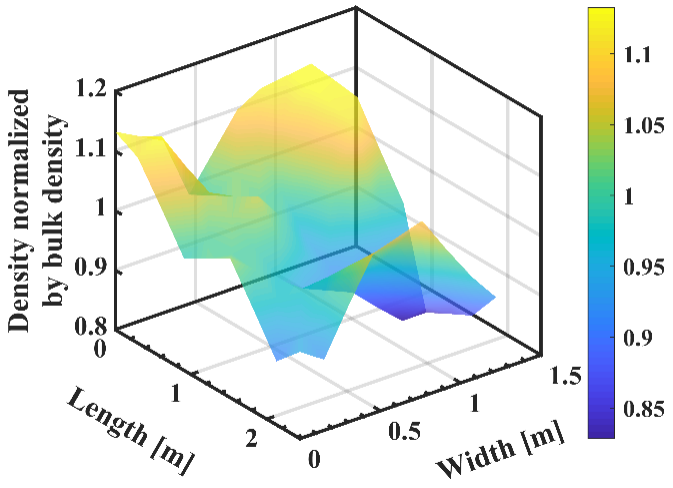

Figure 5. Fractional density variation across an OSB panel surface.

4.1.2 Variation of density across thickness

The two sides of the OSB panels had clear differences in appearance and texture, which was likely to be associated with the manufacturing process. These differences were noted by labeling one side as “smooth” and the other as “rough”, as illustrated in Figure 6. It was also found that the panel density varied considerably across thickness. The average results of these density measurements, which were performed twice, are summarized in Figure 7. OSB density variation across thickness was also observed in previous studies [8, 34]. However, unlike in the current study, where density was found to monotonically decrease from smooth to rough side, the authors of these studies indicated that the density variation had a U-shaped profile.

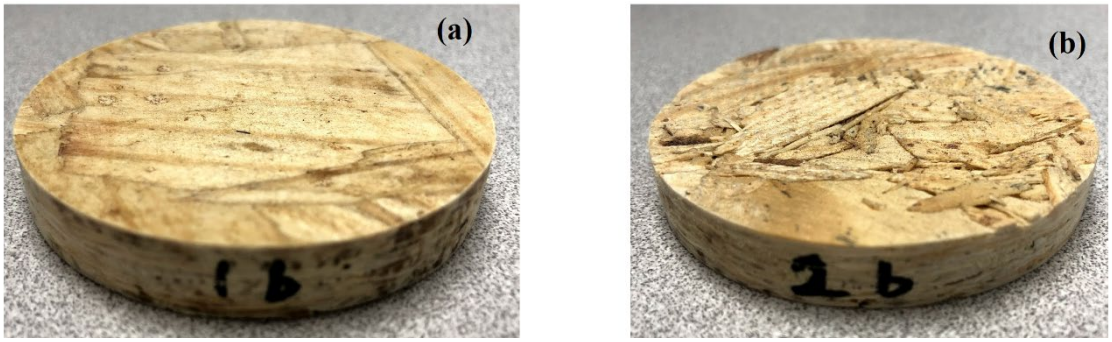

Figure 6. Photographs of CAPA II OSB samples with (a) smooth side and (b) rough side facing the camera.

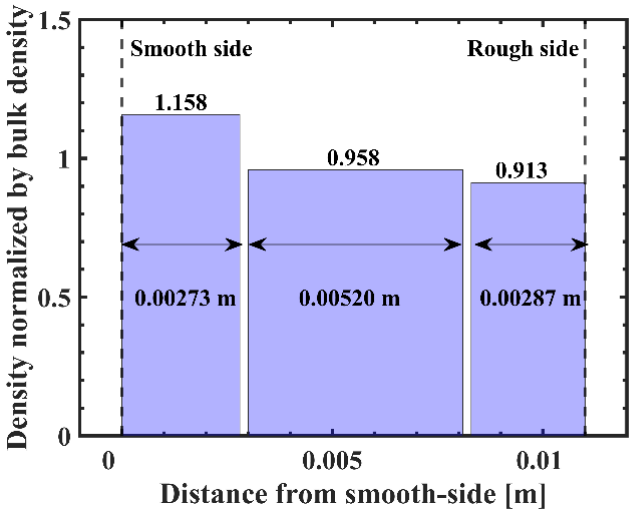

Figure 7. Fractional density variation across the thickness of the OSB panels.

4.2 Results milligram-scale experiments and modeling

4.2.1 TGA/DSC data analysis and model development

Figure 8 presents the mean mass, MLR, heat flow, and integral of heat flow normalized by the initial mass (m_0) obtained in the experiments performed at 10 K min^{-1}. The uncertainties in the experimental data (shown as open circles) were calculated from the scatter of the data as 2 standard deviations of the mean. The reproducibility of the TGA results is excellent throughout, while the scatter of the DSC data increases with increasing temperature due to reduction in the sample mass and increasing baseline uncertainties.

Five reactions can be identified from the MLR curve in Figure 8 (b): the first peak located below 400 K, the asymmetric shoulder of the main peak, the main peak, the minor peak at about 700 K, and the slowly decaying segment above 750 K. The first peak can be attributed to vaporization of chemically-bound water whose mass

fraction is around 1.9 %. The peaks associated with the second to fourth reactions can be identified from the MLR and heat flow curves to be located at 540, 625 and 700 K, respectively. These peaks can also be identified using the second derivative of thermogravimetry (DDTG) curve proposed by Li et al. [13-14] to distinguish overlapping reactions. These and the last reaction can be attributed to the thermal decomposition of wood strands and adhesive.

As the experimental heat flow data in Figure 8 (c) indicate, the first 3 reactions are either endothermic or thermally neutral, but the 4th reaction is clearly exothermic. The presence of exothermic steps in the decomposition of charring polymeric solids was first observed and explained by Li and Stoliarov [10]. Atreya et al. [35] found that wood particle pyrolysis consisted of an endothermic phase followed by an exothermic phase, which is consistent with the presented data.

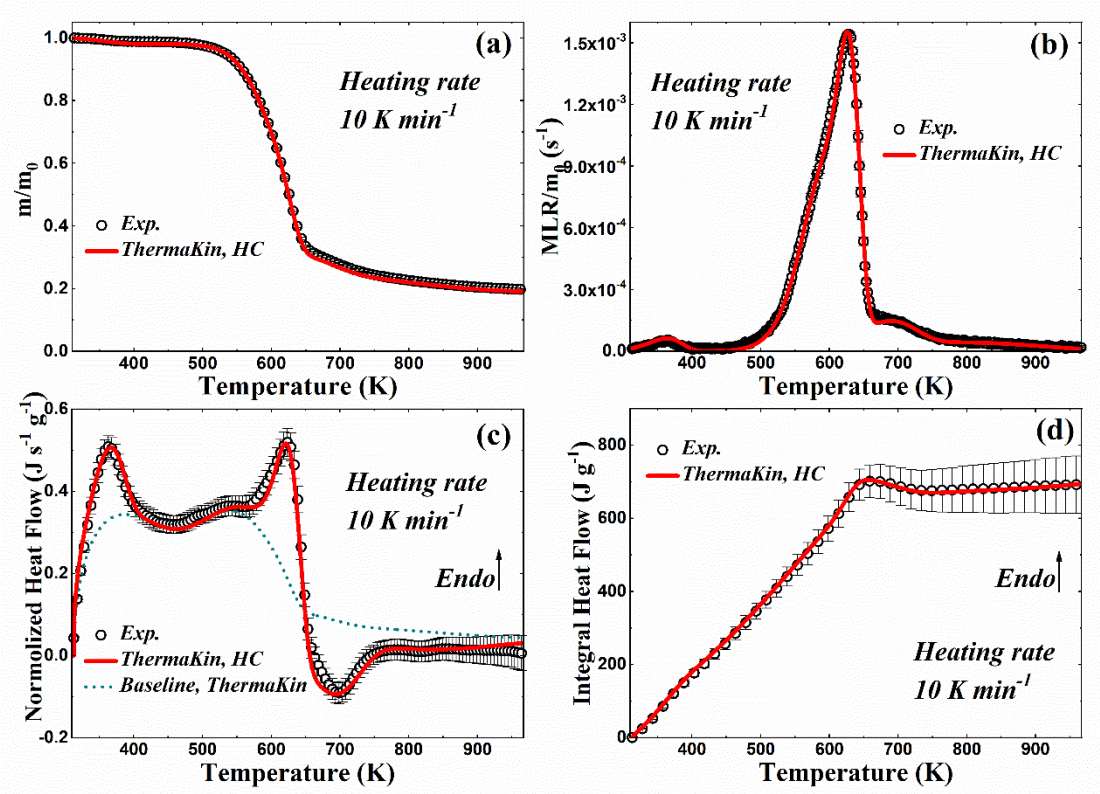

Figure 8. Experimental and simulated TGA ((a), (b)) and DSC ((c), (d)) data obtained for OSB at 10 K min^{-1}.

In majority of earlier studies of engineered wood products [7, 8], thermal decomposition models were formulated using a parallel reaction scheme. The assumption of parallel reactions is consistent with a multi-component nature of these lignocellulosic solids. However, this assumption also yields a requirement for the composition of the undecomposed material (initial concentration of individual components) to be specified. This composition is usually unknown and thus has to be obtained through optimization. Therefore, a decision was made to represent the thermal decomposition of OSB using a set of consecutive reactions, as shown in Table 5 (the stoichiometric coefficients reported in this table were obtained from optimization as discussed later in this section). The only parallel reaction that was used was the reaction that defined the loss of moisture. Using consecutive reactions allowed us to capture the experimental data with the minimum number of adjustable parameters and, thus, follow a widely adopted approach of the minimum complexity.

Heat capacity, C_p, of the OSB component (representing undecomposed OSB) was obtained from the segment of DSC curve located between water vaporization and onset of decomposition, as shown in Figure 9 (a), by dividing the measured heat flow by the instantaneous heating rate. The resulting heat capacity data were subsequently fitted with a linear function of temperature, as shown in Figure 9 (b). The heat capacity of the final residue or char (represented by component Char in Table 3) was obtained in a similar manner. The heat capacity of water was obtained from the literature [36]. The heat capacities of intermediate condensed-phase components

could not be calculated directly and were assigned the values that interpolated between the heat capacities of the OSB and Char components in equal steps. All heat capacity data are summarized in Table 6, and the heats of capacities had estimated uncertainties of 15%.

Table 5. A reaction mechanism for the thermal decomposition of OSB (1.9 wt.% Water + 98.1 wt.% OSB component).

Reaction #	Reaction Equation
1	Water → Water_vapor
2	OSB → 0.72 OSB_INT1 + 0.28 OSB_gas1
3	OSB_INT1 → 0.45 OSB_INT2 + 0.55 OSB_gas2
4	OSB_INT2 → 0.77 OSB_INT3 + 0.23 OSB_gas3
5	OSB_INT3 → 0.77 Char + 0.23 OSB_gas4

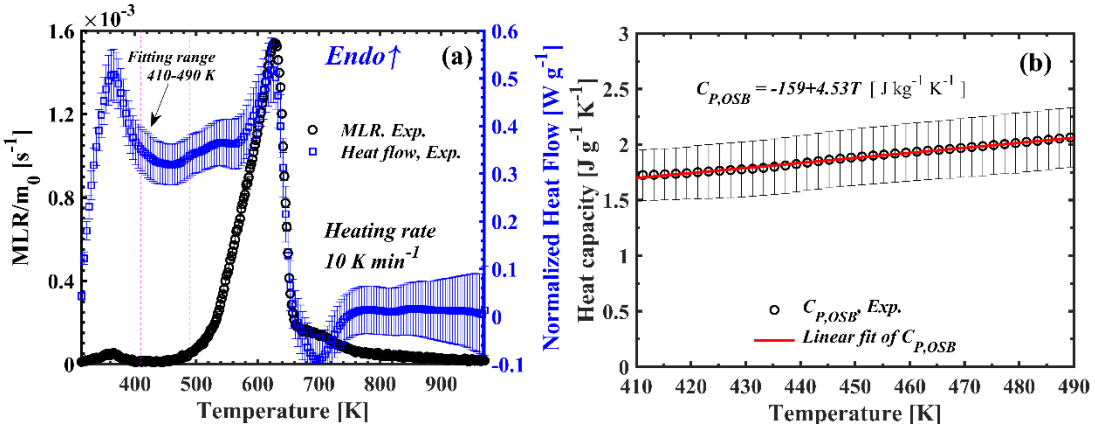

Figure 9. Determination of the heat capacity of undecomposed OSB.

Table 6. Heat capacities of all condensed-phase components.

Component	C_p (J kg^{-1} K^{-1})
Water	5200-6.7T+0.011T^2
OSB	-159+4.53T
OSB_INT1	197+3.40T
OSB_INT2	553+2.27T
OSB_INT3	909+1.13T
Char	1270

All reactions were assumed to be of the first order and their parameters, including *A, E, the heat of reaction, h,* and stoichiometric coefficients were optimized to fit the experimental data at 10 K min^{-1}. The modeled curves shown in Figure 8 capture the TGA and DSC data well within the uncertainties of the measurements. The reaction parameters are given in Table 5 and 7. The estimated uncertainties in *A, E,* and stoichiometric coefficients were studied in previous study [13] where a similar methodology was used. The estimated uncertainties in *A* were ±50%, in *E* were ±3%, in *h* were ±20%, and in the stoichiometric coefficients were ±5%.

Table 7. Optimized thermal decomposition reaction parameters obtained for OSB.

Reaction #	A (s^{-1})	E (J mol^{-1})	h (J kg^{-1}) (+exo)
1	1.55×10^4	4.35×10^4	-2.78×10^6
2	1.56×10^7	1.04×10^5	-6.82×10^3
3	2.65×10^{12}	1.74×10^5	-1.37×10^5
4	8.93×10^3	8.37×10^4	2.90×10^5
5	4.40×10^{-1}	3.86×10^4	2.32×10^5

The heat of vaporization of water was optimized rather than taken from the literature because it was hypothesized to be affected by Van der Waals interactions between water molecules and wood components. Consistent with this hypothesis, the heat of vaporization was found to be about 20% higher in absolute value than that of pure water [37]. Figure 8 (c) shows the calculated sensible heat flow baseline, which helps delineate the endothermic and exothermic phases of the OSB decomposition represented by reactions 2-3 and 4-5, respectively. This baseline was computed by running the model with all heats of reaction set to 0. Excluding the contribution from water, the overall OSB decomposition process is essentially thermally neutral (the net heat of decomposition of 4.6×10^4 J kg^{-1}).

4.2.2 Thermal decomposition model validation and comparison with the models available in the literature

The ability of the model to make predictions at alternate heating rates is demonstrated in Figure 10. The predicted mass and MLR curves match the experimental results well, which intrinsically suggests that the presence of lids and/or changes in the crucible material had no impact on the decomposition kinetics. The model also accurately predicted the final residue yield obtained in the TGA experiments performed at a significantly higher heating rate. Two additional TGA tests were carried out at 50 K min^{-1} in nitrogen to determine whether the residue yield displayed any significant dependence on heating rate. The residue yield did not show any heating rate dependence, which was accurately predicted by the model.

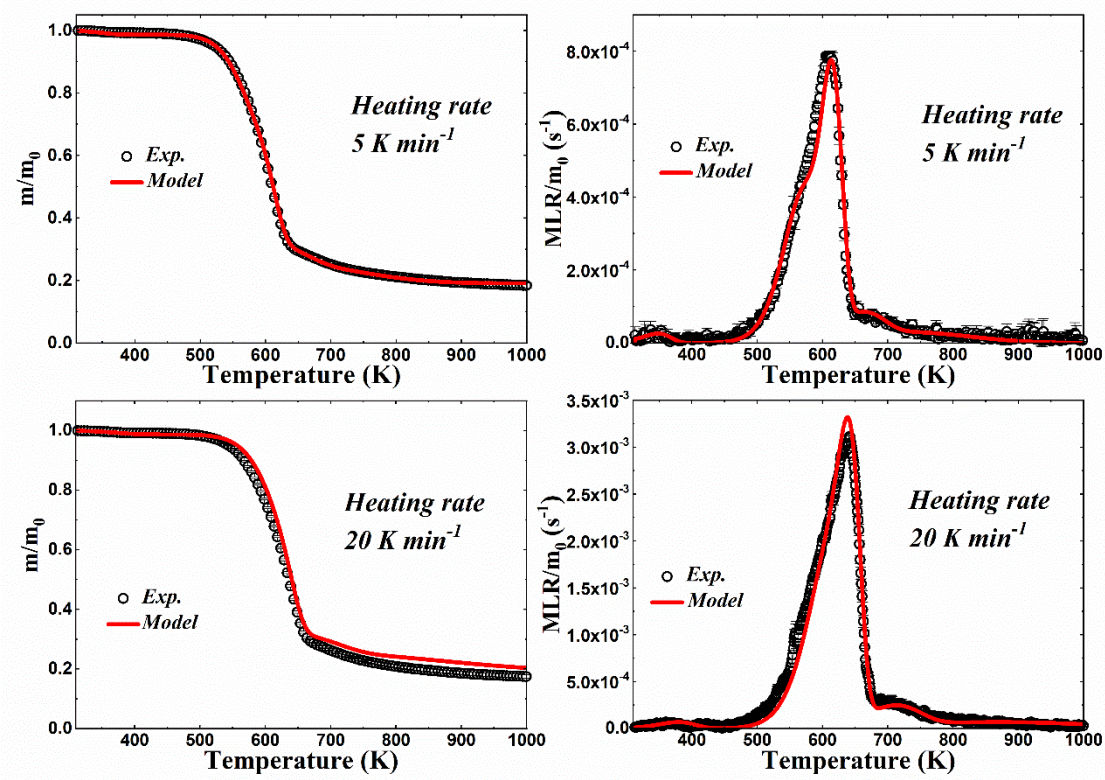

Figure 10. Experimental and simulated TGA data obtained for OSB at 5 K min^{-1} and 20 K min^{-1}.

The OSB decomposition kinetics developed in this work was compared with several literature models obtained for wood [6], OSB [8], MDF [7], softwood [38], and spruce and pine [39]. Grønli et al. [6] collected the TGA data for four hardwoods and five softwoods and proposed a decomposition mechanism consisting of three parallel reactions: one for hemicellulose, one for cellulose, and one for lignin. A set of average kinetic parameters for the nine selected wood species was derived. Ira et al. [8] studied the pyrolysis of six engineered wood products, including an OSB, and also used a three-component parallel reaction scheme to model their measurements. Li et al. [7] examined the thermal decomposition of MDF with additional

consideration for resin (used as a binder) and utilized a four-component parallel reaction scheme as described in section 1.2. By compiling the pyrolysis data from the literature, Richter et al. [38] systematically investigated the effect of chemical composition on charring of softwood at both microscale and mesoscale using a three-component multiple-step reaction scheme. The average composition of softwood was determined to be 47, 24 and 29 wt.% of cellulose, hemicellulose and lignin, respectively. Rinta-Paavola and Hostikka [39] used a four-component parallel reaction mechanism to model TGA, DSC and MCC data collected for spruce and pine.

Figure 11 shows the results of simulations of idealized TGA experiments performed at 5 and 20 K min^{-1} heating rates using all these models, including the model developed in this work. In these simulations, the heating rate was maintained perfectly constant throughout the heating process. Given a wide range of materials these models represent, the results are remarkably similar. Both the positions and shapes of the MLR peaks are very close and the final residue yields vary by only a few wt.%. This comparison suggests that, despite significant differences in the appearance and mechanical properties, the wood products used in the built environment have similar composition and the additives (including adhesives) are present in such low amounts that they do not significantly impact the overall thermal decomposition dynamics.

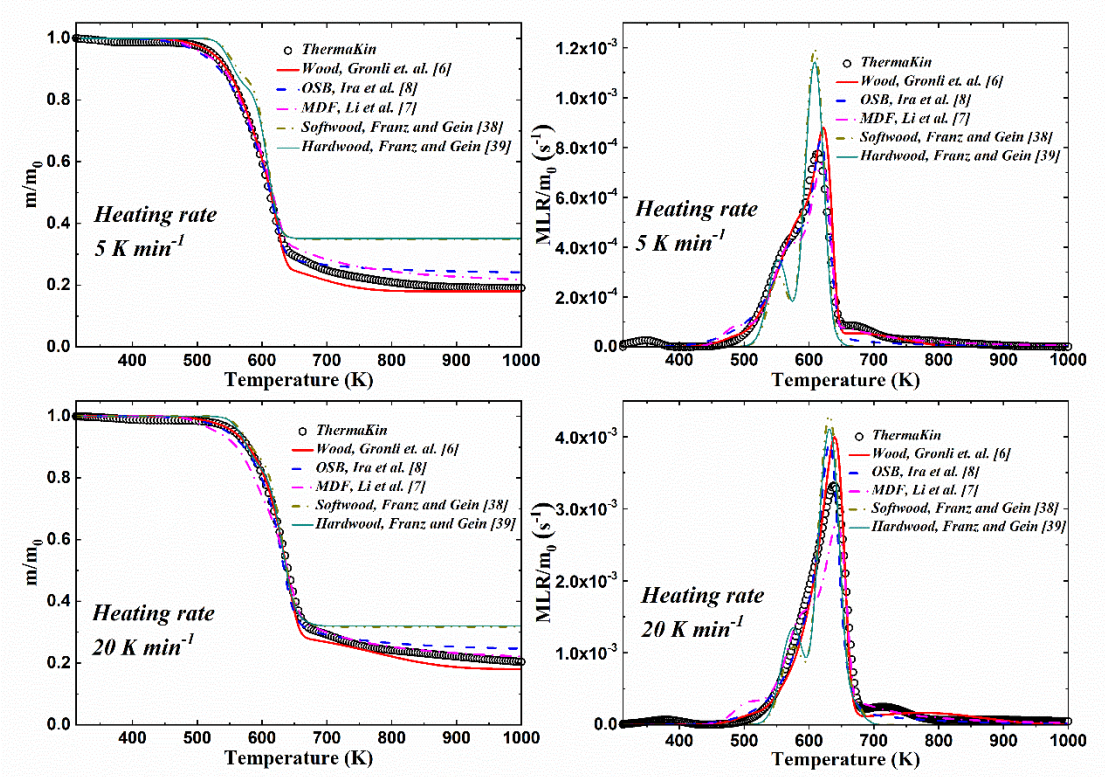

Figure 11. Comparison of mass and MLR data obtained for simulated idealized TGA conducted at 5 and 20 K min^{-1} using the current and literature models for wood and engineered wood products.

4.2.3 MCC data analysis

The heats of combustion, h_c, of the evolved gases defined in the OSB reaction mechanism were determined through modeling of the MCC data. First, the modeled MLR and experimental HRR were compared as shown in Figure 12. A slight mismatch between these signal profiles was identified and corrected by shifting the experimental MCC data by 12.5 K toward the higher temperature. This discrepancy was attributed to a non-uniformity in the temperature of the sample associated with additional heating of its top surface by radiation from the combustor, which was not

fully captured by the MCC sample temperature sensor (located underneath the sample crucible).

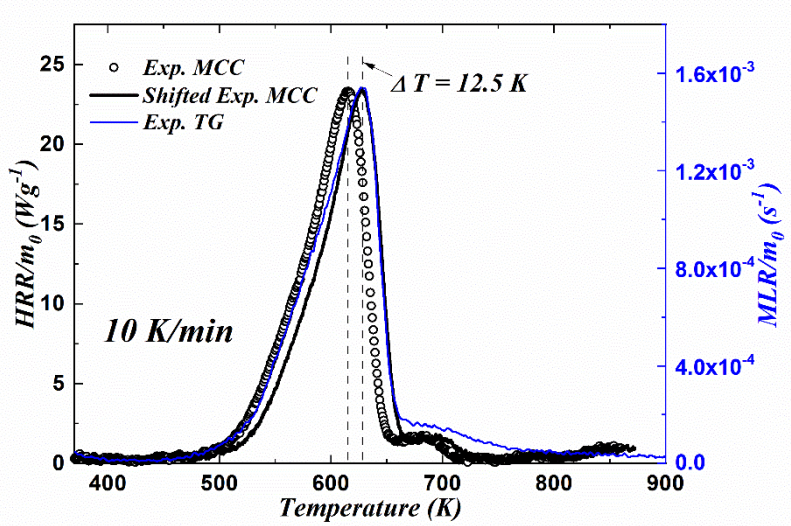

Figure 12. Comparison of unmodified and shifted average experimental HRR data with modeled MLR.

During further analysis, MCC HRR data were generated from the modeling results by first assigning 1×10^7 J kg^{-1} heat of combustion value to all gases. Subsequently, these values were modified iteratively until the experimental average MCC data were matched by the model in accordance with a prescribed set of fitting criteria. These criteria were developed in earlier studies [13 - 14] and comprised less than 5%, 5 K and 5% difference in the maximum HRR, temperature of the maximum and final integral HRR value, respectively. It was determined that it was impossible to satisfy these criteria using a single value of the heat of combustion. Therefore, individual heats of combustion were assigned to individual gases. These heats of combustion are listed in Table 8. The predicted HRR and integral HRR are compared with the corresponding experimental results in Figure 13. The model shows nearly

perfect agreement with the experiments. The net heat of combustion (the total heat released per unit mass gasified) predicted by the model, 1.31×10^7 J kg^{-1}, is close to the value measured for OSB in a cone calorimeter, 1.17×10^7 J kg^{-1} [6] and to the values measured for spruce and pine, $\approx 1.4 \times 10^7$ J kg^{-1}, in an MCC [39**Error! Bookmark not defined.**].

Table 8. Heats of combustion of gaseous decomposition products.

Component	h_c (J kg^{-1})
Water_vapor	0
OSB_gas1	1.25×10^7
OSB_gas2	1.52×10^7
OSB_gas3	1.15×10^7
OSB_gas4	0.75×10^7

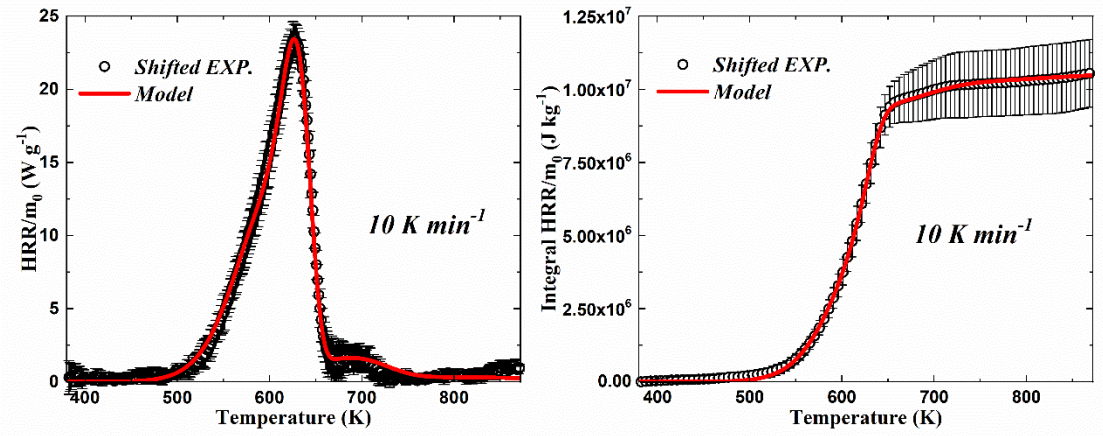

Figure 13. Comparison between the average experimental and simulated MCC data.

4.3 Results of CAPA II experiments and modeling

4.3.1 Preliminary tests: examination of the effect of sample orientation

Eight preliminary CAPA II tests were conducted to determine whether the sample orientation in the apparatus (smooth versus rough side exposed to the heater) and moderate variation in bulk density (within one standard deviation of the mean) significantly impact the test outcomes. The results of these tests are shown in Figure 14. At 35 kW m^{-2}, neither exposure side nor bulk sample density (listed on the figure) appear to have a significant impact on T_{back} or MLR profile. At 65 kW m^{-2}, the choice of exposure side still shows no significant impact. However, the density does appear to have a detectable impact: the second MLR peak shifts slightly to a later time with increasing density.

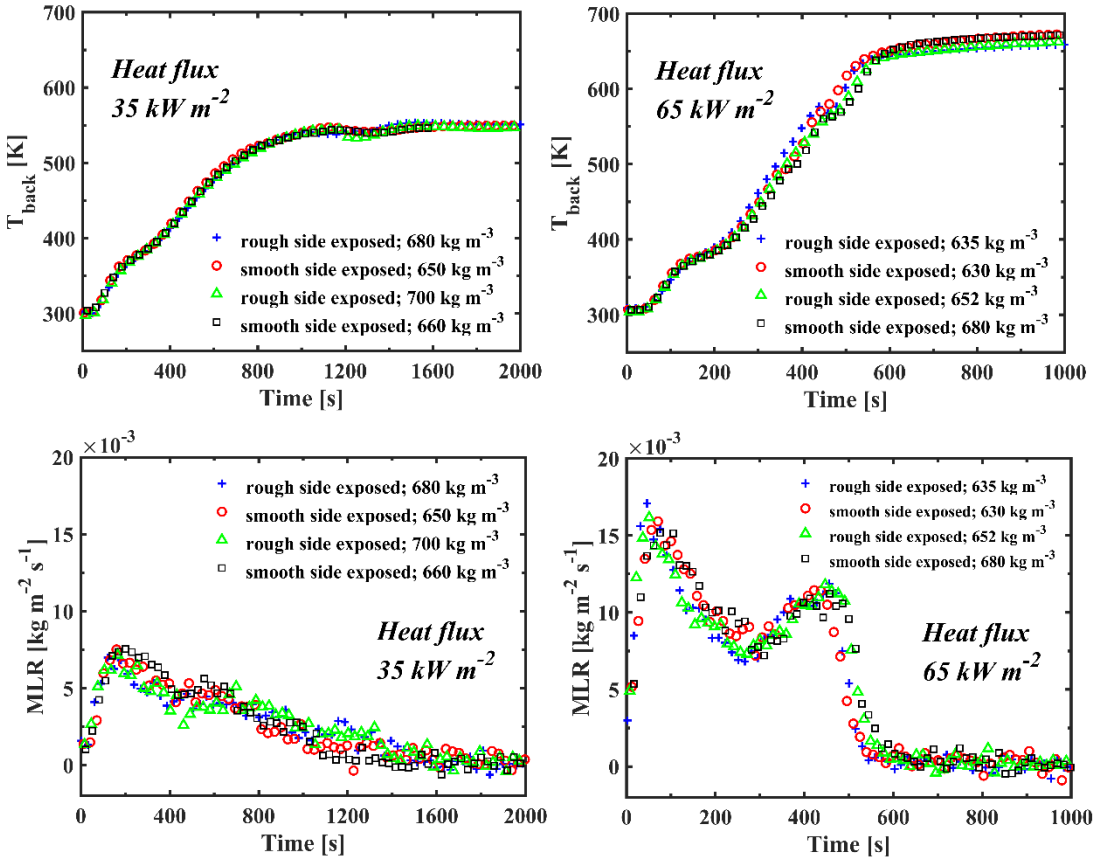

Figure 14. Preliminary CAPA II measurement results obtained for samples exposed to 35 kW m^{-2} and 65 kW m^{-2} of radiant heat flux with either smooth or rough side facing the heater.

4.3.2 Determination of thermal transport parameters

Two final CAPA II tests were performed at 35 kW m^{-2} of radiant heat flux and anther two were performed at 65 kW m^{-2} of radiant heat flux to be used in the model parameterization and validation. In these tests, all samples were oriented with the rough side facing the heater because the smooth side was believed to provide a better thermal contact with the copper foil. The samples used in the repeated tests at the same radiant heat flux setting were selected to have similar density so that the test

results could be combined into a single data set. The average T_{back} data obtained at 65 kW m^{-2} of radiant heat flux were selected as a target for thermal conductivity determination because preliminary tests indicated that the OSB samples did not fully decompose at 35 kW m^{-2}.

The OSB and its condensed-phase decomposition products (listed in Table 6) were defined in the model as not transparent to radiation. The emissivities of these components were specified using the results of the measurements performed by Försth and Roos [23] on a similar EWP, plywood. According to these measurements, for a 1025 K gray body radiation (which approximately corresponds to a cone calorimetry heater setting of 50 kW m^{-2}), this emissivity for undecomposed plywood was 0.81. This emissivity was found to decrease to about 0.70 after a prolonged exposure to 30 kW m^{-2} of cone heater radiation. Based on these observations, the OSB and condensed-phase decomposition product emissivities were defined as shown in Table 9. The heat capacities of all gaseous OSB decomposition products (listed in Table 8) were assumed equal to 2100 J kg^{-1} K^{-1}, which was the mean heat capacity of a collection of C1 to C8 hydrocarbons at a temperature of 600 K [25]. The heat capacity of the water vapor was obtained from the literature [36].

Table 9. Broad band emissivities of condensed-phase components of OSB.

Component	Emissivity
OSB	0.81
OSB_INT1	0.78
OSB_INT2	0.76
OSB_INT3	0.73

Char	0.70

Two versions of the OSB pyrolysis model were formulated. In the first version, referred to as uniform density model, the OSB sample was assumed to always have the average density (664 kg m^{-3}). The densities of condensed-phase decomposition products of OSB were subsequently defined to reproduce the preliminary CAPA II test observations that all samples expanded in thickness by about 1.6 mm (15 %) upon decomposition. These densities are listed in Table 10. Note that the density of the undecomposed OSB component does not exactly equal to the average density of the panel (664 kg m^{-3}) because the OSB sample also contains 1.9 wt.% of chemically bound water (Water component) that is assumed to contribute to mass but not volume of the OSB panel.

In the second version of the model, referred to as non-uniform density model, the OSB density variation through thickness and from sample to sample was taken into account by defining undecomposed OSB as a mixture of two components: OSB1 and OSB2. These two components had different densities, 800 and 550 kg m^{-3}, respectively, with all other properties being the same. As in the case of uniform density model, the densities of condensed-phase products derived from OSB1 and OSB2 were selected to reproduce the experimentally observed expansion in the OSB thickness upon decomposition. These density values are summarized in Table 10. The sample was modeled as a three-layer composite with each layer having different initial mass fractions of OSB1 and OSB2. These mass fractions were selected to

capture the measured density distribution thorough thickness given in Figure 7 and to match the average bulk density of the samples used in the target experiments.

Table 10. Densities of condensed-phase components of OSB in kg m^{-3}.

Component	Uniform density model: OSB	Non-uniform density model: OSB1	Non-uniform density model: OSB2
OSB	652	800	550
OSB_INT1	468	573	394
OSB_INT2	184	226	156
OSB_INT3	142	174	120
Char	108	133	91

The thermal conductivities of all condensed-phase components were assumed to be independent of temperature to minimize the number of adjustable parameters and were optimized to capture the mean experimental T_{back} obtained at 65 kW m^{-2} shown in Figure 15. The uncertainties in the experimental T_{back} were computed from the scatter of the data as two standard deviations of the mean. In the case of the non-uniform density model, e the number of adjustable thermal conductivities was kept the same as in the uniform density model by assigning the same values to the corresponding components derived from OSB1 and OSB2. The Water component was set not to contribute to the thermal conductivity of the sample. The optimized T_{back} profiles are shown in Figure 15; the corresponding thermal conductivity values are summarized in Table 11, and the approximate uncertainties were ±8%. The uncertainties were determined by changing thermal conductivities in the model while

still providing acceptable agreement between the model prediction and the experimental curves. Both models capture the experimental data well.

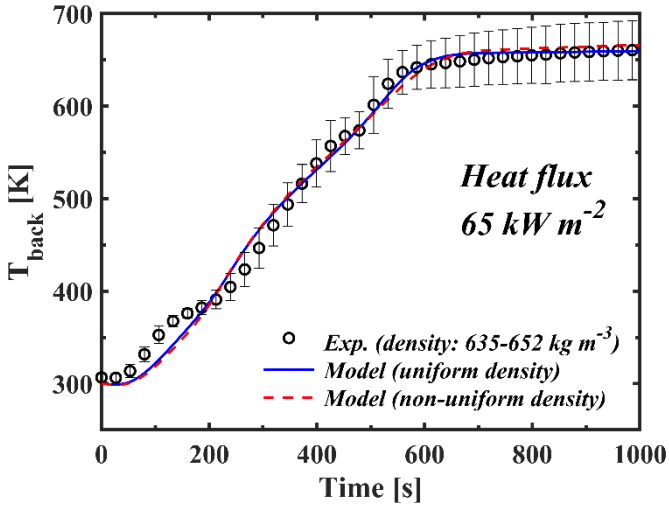

Figure 15. Comparison of the experimental and simulated OSB sample T_{back} profiles obtained in CAPA II tests at 65 kW m^{-2}.

Table 11. Optimized thermal conductivities in W m^{-1} K^{-1} of condensed-phase components of OSB.

Component	Uniform density model	Non-uniform density model: OSB1 and OSB2
OSB	0.13	0.13
OSB_INT1	0.06	0.10
OSB_INT2	0.42	0.35
OSB_INT3	0.39	0.39
Char	0.53	0.62

4.3.3 Complete pyrolysis model validation

A comparison of the modeled and average experimental MLR obtained in the CAPA II tests performed at 65 kW m^{-2} is given in Figure 16. A comparison of the he modeled and average experimental T_{back} and MLR obtained at 35 kW m^{-2} is shown in Figure 17. Both models (uniform and non-uniform density) capture the MLR maxima at both heat fluxes well. Both models significantly underestimate the magnitude of the second, smaller MLR peak observed at 65 W m^{-2}. The 35 kW m^{-2} experimental T_{back} data are captured well by both models for the first 1000 s and are overpredicted by both models at later times. The results indicate that the non-uniform density model, where the density variation across sample thickness and from sample to sample are resolved, does not offer a significant improvement in the overall predictions. Therefore, a simpler, uniform density model is recommended.

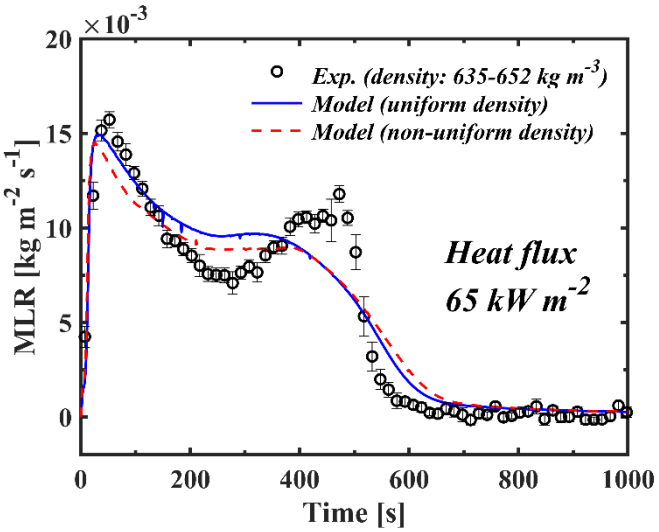

Figure 16. Comparison of the experimental and simulated OSB MLR profiles obtained in CAPA II tests at 65 kW m^{-2}.

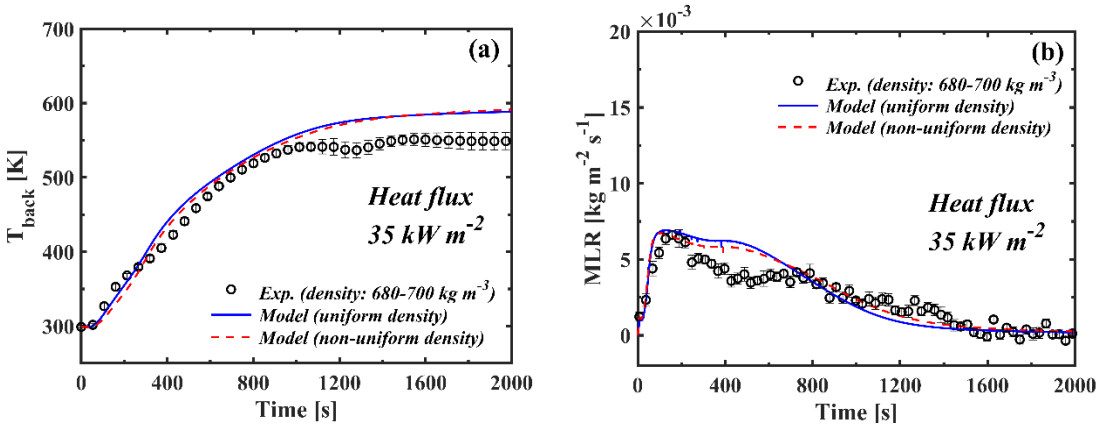

Figure 17. Comparison of the experimental and simulated OSB (a) sample T_{back} and (b) MLR profiles obtained in CAPA II tests at 35 kW m^{-2}.

4.3.4 Further discussion of modeling results

The underestimation of the second, smaller MLR peak observed in the CAPA II tests performed at 65 W m^{-2} by the models was significant and warranted further scrutiny. Several potential reasons for this discrepancy were considered. First, it was hypothesized that a movement of gaseous decomposition products through the OSB was inhibited at the early stages of its decomposition (corresponding to OSB, OSB_INT1 and OSB_INT2 components), which may have enhanced the mass loss at the late stages of pyrolysis. However, it was found that the model, where such transport limitation was introduced, did not show a significantly improvement in the prediction and the experimental MLR. Second, several variations in the density profiles through sample thickness were examined. For example, it was assumed that the density of the OSB within the two outer layers shown in Figure 7 is in fact non-uniform with most of the material concentrated near the sample surfaces. Again, none

of the considered density variations resulted in significant improvements in the model predictions.

Finally, a closer analysis of the video footage collected during the CAPA II experiments was performed and revealed that the OSB samples had a tendency to shrink in diameter at the late stages of pyrolysis. This shrinkage was especially significant in the tests performed at 65 kW m^{-2}. Figure 18 shows a picture of a sample before test and a decomposed sample after CAPA II test at 65 kW m^{-2}. This shrinkage resulted in decoupling of the sample from the side insulator and exposure of the side of the sample to the radiation from the heater. This exposure, which was not captured in the current models, was likely to be at least partially responsible for the increased magnitude of the second MLR peak observed in the CAPA II experiments. Multiple attempts to mitigate this shrinkage by securing the sample to the copper foil and supporting aluminum mesh were unsuccessful.

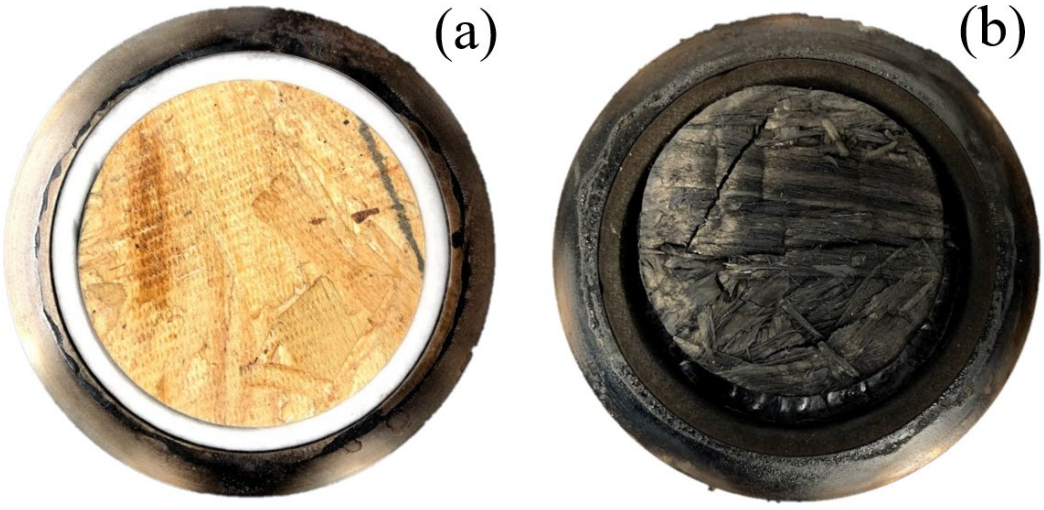

Figure 18. Photograph of OSB samples (a) before and (b) after CAPA II tests at 65 kW m^{-2}.

The results of the preliminary CAPA II tests discussed in Section 4.3.1 and presented in Figure 14 showed that the second MLR peak observed at 65 kW m^{-2} shifted to a later time with increasing OSB panel density. To see if the current model predicts this shift, two additional simulations were performed with the OSB component density set to either 550 kg m^{-3} or 752 kg m^{-3} (the minimum and maximum OSB panel density measured in the current study). The densities of all condensed-phase products of uniform density model given in Table 10 were scaled, accordingly. The results of these simulations are presented in Figure 19. They show that this model qualitatively reproduced the trend observed in the experiments.

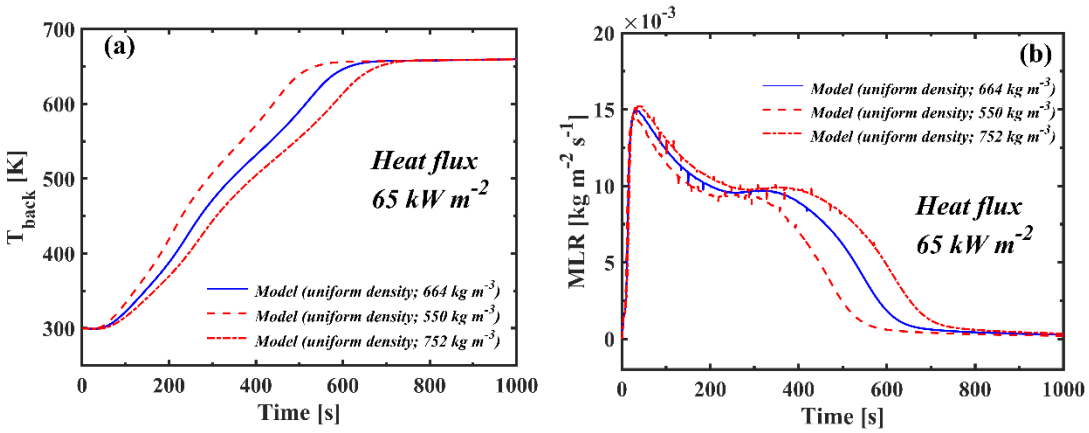

Figure 19. Analysis of impact of varation in bulk sample density on 65 kW m^{-2} CAPA II test simulation results.

Chapter 5: Conclusions

In this work, a pyrolysis model for Oriented Strand Board (OSB) has been developed. The OSB thermal decomposition consisted of a water vaporization step and four consecutive, first order reactions representing the decomposition of organic constituents of this material. This mechanism was developed using TGA and DSC tests performed at a nominal heating rate of 10 K min^{-1}. These tests were analyzed with a numerical model, ThermaKin2Ds, coupled with an *HC* optimization algorithm to determine the relevant kinetic and thermodynamic parameters. This parameter set was shown to accurately reproduce additional TGA data obtained at alternate heating rates of 5 and 20 K min^{-1}, which provided the necessary validation.

A series of MCC tests was also performed on this material. Modeling these tests yielded the heats of combustion of gaseous products of the decomposition reactions. These heats of combustion were found to vary between the reaction steps. 5 and 20 K min^{-1} idealized TGA profiles obtained with the current model were compared with those generated using the decomposition models of wood and engineered wood products available in the literature. All profiles were found to be remarkably similar indicating similarity in the chemical composition.

Gram-scale gasification experiments were conducted using CAPA II and analyzed through inverse modeling with the ThermaKin2Ds coupled with an *HC* optimization algorithm. A uniform density and a non-uniform density pyrolysis models were developed, and the thermal conductivity of the condensed-phase components were determined through fitting of the experimental T_{back} profiles

obtained at 65 kW m^{-2} of radiant heat flux. No obvious difference was found between the performances of these two models. Both models reproduced the T_{back} at 65 kW m^{-2}, and first 1000 s of the temperature history at 35 kW m^{-2} well. Both models captured the main MLR maxima at 35 and 65 kW m^{-2}. However, there was a clear discrepancy in the magnitude of the second MLR peak, which was attributed imperfections in the experimental measurements.

Appendices I: Summary of Material Properties

Uniform density model

Condensed phase components	Density [kg m^{-3}]	Heat capacity [J kg^{-1} K^{-1}]	Thermal conductivity [W m^{-1} K^{-1}]	Gas transfer coefficient [m^2 s^{-1}]	Emissivity [/]
OSB	652	-159+4.53T	0.13	2×10^{-5}	0.81
OSB_INT1	468	197+3.4T	0.06	2×10^{-5}	0.78
OSB_INT2	184	553+2.27T	0.42	2×10^{-5}	0.76
OSB_INT3	142	909+1.13T	0.39	2×10^{-5}	0.73
Char	108	1265	0.53	2×10^{-5}	0.70
Gaseous components					
OSB_gas1	664	2100	0.2	2×10^{-5}	0.81
OSB_gas2	664	2100	0.2	2×10^{-5}	0.81
OSB_gas3	664	2100	0.2	2×10^{-5}	0.81
OSB_gas4	664	2100	0.2	2×10^{-5}	0.81

Other components					
WATER	10000	$5.2\times10^{-3}-6.7\times T+1.1\times10^{-2}\times T^2$	0.13	2×10^{-5}	0.81
WATER_VAPOR	10000	$2.4\times10^{-3}-1.6\times T+2.0\times10^{-2}\times T^2$	0.2	2×10^{-5}	0.81

Reaction #	Reaction Equation	A [s^{-1}]	E [J mol^{-1}]	h [J kg^{-1}] (+exo)
1	Water → Water_vapor	1.55×10^4	4.35×10^4	-2.78×10^6
2	OSB → 0.72 OSB_INT1 + 0.28 OSB_gas1	1.56×10^7	1.04×10^5	-6.82×10^3
3	OSB_INT1 → 0.45 OSB_INT2 + 0.55 OSB_gas2	2.65×10^{12}	1.74×10^5	-1.37×10^5
4	OSB_INT2 → 0.77 OSB_INT3 + 0.23 OSB_gas3	8.93×10^3	8.37×10^4	2.90×10^5
5	OSB_INT3 → 0.77 CHAR + 0.23 OSB_gas4	4.40×10^{-1}	3.86×10^4	2.32×10^5

Non-uniform density model

Condensed phase component	Density [$kg\ m^{-3}$]	Heat capacity [$J\ kg^{-1}\ K^{-1}$]	Thermal conductivity [$W\ m^{-1}\ K^{-1}$]	Gas transfer coefficient [$m^2\ s^{-1}$]	Emissivity [/]
OSB1	800	-159+4.53T	0.13	2×10^{-5}	0.81
OSB2	550				

OSB1_INT1 OSB2_INT1	574 394	197+3.4T	0.10	2×10-5	0.78
OSB1_INT2 OSB2_INT2	226 155	553+2.27T	0.35	2×10-5	0.76
OSB1_INT3 OSB2_INT3	174 120	909+1.13T	0.39	2×10-5	0.73
CHAR1 CHAR2	133 91	1265	0.62	2×10-5	0.70
Gaseous component					
OSB1_gas1 OSB1_gas2 OSB1_gas3 OSB1_gas4	800	2100	0.2	2×10^{-5}	0.81
OSB2_gas1 OSB2_gas2 OSB2_gas3 OSB2_gas4	550	2100	0.2	2×10^{-5}	0.81

Reaction #	Reaction Equation	A [s^{-1}]	E [J mol^{-1}]	h [J kg^{-1}] (+exo)
1	Water → Water_vapor	1.55×10^{4}	4.35×10^{4}	-2.78×10^{6}
2_1	OSB1 → 0.72 OSB1_INT1 + 0.28 OSB1_gas1	1.56×10^{7}	1.04×10^{5}	-6.82×10^{3}
2_2	OSB2 → 0.72 OSB2_INT1 + 0.28 OSB2_gas1			
3_1	OSB1_INT1 → 0.45 OSB1_INT2 + 0.55 OSB1_gas2	2.65×10^{12}	1.74×10^{5}	-1.37×10^{5}
3_2	OSB2_INT1 → 0.45 OSB2_INT2 + 0.55 OSB2_gas2			
4_1	OSB1_INT2 → 0.77 OSB1_INT3 + 0.23 OSB1_gas3	8.93×10^{3}	8.37×10^{4}	2.90×10^{5}
4_2	OSB2_INT2 → 0.77 OSB2_INT3 + 0.23 OSB2_gas3			
5_1	OSB1_INT3 → 0.77 CHAR1 + 0.23 OSB1_gas4	4.40×10^{-1}	3.86×10^{4}	2.32×10^{5}
5_2	OSB2_INT3 → 0.77 CHAR2 + 0.23 OSB2_gas4			

Bibliography

[1] Howard, J., Liang, S. (July 2019). U.S. Timber Production, Trade, Consumption, and Price Statistics, 1965–2017. *Res. Pap. FPL-RP-701. Madison, WI: U.S. Department of Agriculture, Forest Service, Forest Products Laboratory: 1-106.*

[2] Marotte, B. (2016, July 19). *Toronto's Norbord riding the rising wave of OSB sales*. The Globe and Mail. https://www.theglobeandmail.com/report-on-business/forest-products-firm-norbord-riding-the-rising-wave-of-osb-sales/article30985989/

[3] Suzuki, S., Manzello, S. L., & Hayashi, Y. (2013). The size and mass distribution of firebrands collected from ignited building components exposed to wind. *Proceedings of the Combustion Institute*, *34*(2), 2479–2485. https://doi.org/10.1016/j.proci.2012.06.061

[4] Purnomo, D. M. J., Richter, F., Bonner, M., Vaidyanathan, R., & Rein, G. (2020). Role of optimisation method on kinetic inverse modelling of biomass pyrolysis at the microscale. *Fuel*, *262*, 116251. https://doi.org/10.1016/j.fuel.2019.116251

[5] Shafizadeh, F., & Chin, P. (1977). Thermal Deterioration of Wood. In *Wood Technology: Chemical Aspects (Acs Symposium Series; Number 43))* (1st ed., pp. 57–81). Amer Chemical Society.

[6] Grønli, M. G., Várhegyi, G., & Di Blasi, C. (2002). Thermogravimetric Analysis and Devolatilization Kinetics of Wood. *Industrial & Engineering Chemistry Research*, *41*(17), 4201–4208. https://doi.org/10.1021/ie0201157

[7] Li, K.-Y., Huang, X., Fleischmann, C., Rein, G., & Ji, J. (2014). Pyrolysis of Medium-Density Fiberboard: Optimized Search for Kinetics Scheme and Parameters via a Genetic Algorithm Driven by Kissinger's Method. *Energy & Fuels*, *28*(9), 6130–6139. https://doi.org/10.1021/ef501380c

[8] Ira, J. ř., Hasalová, L., Šálek, V. ě., Jahoda, M., & Vystrčil, V. (2019). Thermal Analysis and Cone Calorimeter Study of Engineered Wood with an Emphasis on Fire Modelling. *Fire Technology*, *56*(3), 1099–1132. https://doi.org/10.1007/s10694-019-00922-9

[9] Fateh, T., Rogaume, T., Luche, J., Richard, F., & Jabouille, F. (2013). Kinetic and mechanism of the thermal degradation of a plywood by using thermogravimetry and Fourier-transformed infrared spectroscopy analysis in nitrogen and air atmosphere. *Fire Safety Journal*, *58*, 25–37. https://doi.org/10.1016/j.firesaf.2013.01.019

[10] Stoliarov, S. I., Safronava, N., & Lyon, R. E. (2009). The effect of variation in polymer properties on the rate of burning. *Fire and Materials*, *33*(6), 257–271. https://doi.org/10.1002/fam.1003

[11] Li, J., & Stoliarov, S. I. (2013). Measurement of kinetics and thermodynamics of the thermal degradation for non-charring polymers. *Combustion and*

Flame, *160*(7), 1287–1297.
https://doi.org/10.1016/j.combustflame.2013.02.012

[12] Li, J., & Stoliarov, S. I. (2014). Measurement of kinetics and thermodynamics of the thermal degradation for charring polymers. *Polymer Degradation and Stability*, *106*, 2–15. https://doi.org/10.1016/j.polymdegradstab.2013.09.022

[13] McKinnon, M., & Stoliarov, S. (2015). Pyrolysis Model Development for a Multilayer Floor Covering. *Materials*, *8*(9), 6117–6153.
https://doi.org/10.3390/ma8095295

[14] McKinnon, M. B., Ding, Y., Stoliarov, S. I., Crowley, S., & Lyon, R. E. (2016). Pyrolysis model for a carbon fiber/epoxy structural aerospace composite. *Journal of Fire Sciences*, *35*(1), 36–61.
https://doi.org/10.1177/0734904116679422

[15] Ding, Y., McKinnon, M. B., Stoliarov, S. I., Fontaine, G., & Bourbigot, S. (2016). Determination of kinetics and thermodynamics of thermal decomposition for polymers containing reactive flame retardants: Application to poly(lactic acid) blended with melamine and ammonium polyphosphate. *Polymer Degradation and Stability*, *129*, 347–362.
https://doi.org/10.1016/j.polymdegradstab.2016.05.014

[16] Kawasaki, T., & Kawai, S. (2006). Thermal insulation properties of wood-based sandwich panel for use as structural insulated walls and floors. *Journal of Wood Science*, *52*(1), 75–83. https://doi.org/10.1007/s10086-005-0720-0

[17] Yoo, J., Chang, S. J., Lee, J., Wi, S., & Kim, S. (2019). Numerical analysis of hygrothermal properties and behavior of Korean based cross-laminated timber (CLT) wall system to deduce optimal assemblies. *Journal of Cleaner Production*, *213*, 1217–1227. https://doi.org/10.1016/j.jclepro.2018.12.221

[18] Kamke, F. A., & Hasselman, D. (2011). THERMAL CONDUCTIVITY OF WOOD-BASED PANELS. In *Thermal Conductivity 20* (Softcover reprint of the original 1st ed. 1989 ed., pp. 249–259). Springer.

[19] Sonderegger, W., & Niemz, P. (2009). Thermal conductivity and water vapour transmission properties of wood-based materials. *European Journal of Wood and Wood Products*, *67*(3), 313–321. https://doi.org/10.1007/s00107-008-0304-y

[20] Czajkowski, Ł., Olek, W. ł., Weres, J., & Guzenda, R. (2016). Thermal properties of wood-based panels: thermal conductivity identification with inverse modeling. *European Journal of Wood and Wood Products*, *74*(4), 577–584. https://doi.org/10.1007/s00107-016-1021-6

[21] McKinnon, M. (2016). A Generalized Methodology to Characterize Composite Materials for Pyrolysis Models [Digital Repository at the University of Maryland]. https://doi.org/10.13016/M2CB6S

[22] Agarwal, G., Chaos, M., & Wang, Y. (2020). Validation of pyrolysis model in transient heating scenarios and diverse spectral boundary conditions. *Fire Safety Journal*, 103064. https://doi.org/10.1016/j.firesaf.2020.103064

[23] Försth, M., & Roos, A. (2010). Absorptivity and its dependence on heat source temperature and degree of thermal breakdown. *Fire and Materials*, *35*(5), 285–301. https://doi.org/10.1002/fam.1053

[24] McKinnon, M. B., Martin, G. E., & Stoliarov, S. I. (2019). Pyrolysis model for multiple compositions of a glass reinforced unsaturated polyester composite. *Journal of Applied Polymer Science*, *137*(2), 47697. https://doi.org/10.1002/app.47697

[25] Swann, J. D., Ding, Y., & Stoliarov, S. I. (2019). Characterization of pyrolysis and combustion of rigid poly(vinyl chloride) using two-dimensional modeling. *International Journal of Heat and Mass Transfer*, *132*, 347–361. https://doi.org/10.1016/j.ijheatmasstransfer.2018.12.011

[26] Swann, J. D., Ding, Y., & Stoliarov, S. I. (2020a). A quantitative comparison of the pyrolysis and combustion behavior of plasticized and rigid poly(vinyl chloride) using two-dimensional modeling. *Fire Safety Journal*, *111*, 102910. https://doi.org/10.1016/j.firesaf.2019.102910

[27] Swann, J. D., Ding, Y., & Stoliarov, S. I. (2020b). Comparative analysis of pyrolysis and combustion of bisphenol A polycarbonate and poly(ether ether ketone) using two-dimensional modeling: A relation between thermal transport and the physical structure of the intumescent char. *Combustion and Flame*, *212*, 469–485. https://doi.org/10.1016/j.combustflame.2019.11.017

[28] Swann, J. D., & Stoliarov, S. I. (2020). Determination of pyrolysis and combustion properties of poly(vinylidene fluoride) using comprehensive modeling: Relating heat transfer to the intumescent char's porous structure. *Fire Safety Journal*, 103086. https://doi.org/10.1016/j.firesaf.2020.103086

[29] Fiola, G. J., Chaudhari, D. M., & Stoliarov, S. I. (2020). Comparison of Pyrolysis Properties of Extruded and Cast Poly(methyl methacrylate). *Fire Safety Journal*, 103083. https://doi.org/10.1016/j.firesaf.2020.103083

[30] Stoliarov, S. I., Leventon, I. T., & Lyon, R. E. (2013). Two-dimensional model of burning for pyrolyzable solids. *Fire and Materials*, *38*(3), 391–408. https://doi.org/10.1002/fam.2187

[31] ASTM Standard D7309, 2013, " Standard Test Method for Determining Flammability Characteristics of Plastics and Other Solid Materials Using Microscale Combustion Calorimetry," ASTM International, West Conshohocken, PA, 2013, DOI: 10.1520/D7309-13, www.astm.org

[32] Lyon, R.E., Walters, R.N., Stoliarov, S.I., & Safronava, N. (2013). Principles and practice of microscale combustion calorimetry. Report No. DOT/FAA/TC-12/53, Federal Aviation Administration. April 2013.

[33] Swann, J. D., Ding, Y., McKinnon, M. B., & Stoliarov, S. I. (2017). Controlled atmosphere pyrolysis apparatus II (CAPA II): A new tool for analysis of pyrolysis of charring and intumescent polymers. *Fire Safety Journal*, *91*, 130–139. https://doi.org/10.1016/j.firesaf.2017.03.038

[34] Pipíška, T. š., Pařil, P., Čermák, P., Dömény, J., Král, P., & Kamke, F. (2020). Effect of chemical and thermal modification, and material replacement on strand board properties. *European Journal of Wood and Wood Products*, *78*(3), 565–575. https://doi.org/10.1007/s00107-020-01527-8

[35] Atreya, A., Olszewski, P., Chen, Y., & Baum, H. R. (2017). The effect of size, shape and pyrolysis conditions on the thermal decomposition of wood particles and firebrands. *International Journal of Heat and Mass Transfer*, *107*, 319–328. https://doi.org/10.1016/j.ijheatmasstransfer.2016.11.051

[36] McKinnon, M. B., Stoliarov, S. I., & Witkowski, A. (2013). Development of a pyrolysis model for corrugated cardboard. *Combustion and Flame*, *160*(11), 2595–2607. https://doi.org/10.1016/j.combustflame.2013.06.001

[37] Incropera FP, DeWitt DP, Bergman TL, Lavine AS. Fundamentals of heat and mass transfer, 6th ed. *Johe Wiley & Sons, Inc; 2007.*

[38] Richter, F., Atreya, A., Kotsovinos, P., & Rein, G. (2019). The effect of chemical composition on the charring of wood across scales. *Proceedings of the Combustion Institute*, *37*(3), 4053–4061. https://doi.org/10.1016/j.proci.2018.06.080

[39] Rinta-Paavola, A., & Hostikka, S. (2019). A Model for Pyrolysis and Oxidation of Two Common Structural Timbers. In T. Kalamees, A. Just, M. Semjonov, A. Teder, & M. Deemant (Eds.), Proceedings of the I Forum Wood Building Baltic, 2019 Tallinn University of Technology.

https://www.ttu.ee/public/k/Konverentsikeskus/A_Model_for_Pyrolysis_and_Oxidation_of_Two_Common_Structural_Timbers.pdf

[40] Zeinali, D., Gupta, A., Maragkos, G., Agarwal, G., Beji, T., Chaos, M., Wang, Y., Degroote, J., & Merci, B. (2019). Study of the importance of non-uniform mass density in numerical simulations of fire spread over MDF panels in a corner configuration. *Combustion and Flame*, *200*, 303–315. https://doi.org/10.1016/j.combustflame.2018.11.020